

# Plate tectonic controls on atmospheric CO<sub>2</sub> levels since the Triassic

Douwe G. Van Der Meer<sup>a,b,1</sup>, Richard E. Zeebe<sup>c</sup>, Douwe J. J. van Hinsbergen<sup>a</sup>, Appy Sluijs<sup>a</sup>, Wim Spakman<sup>a,d</sup>, and Trond H. Torsvik<sup>d,e,f</sup>

<sup>a</sup>Department of Earth Sciences, Utrecht University, 3584 CD, Utrecht, The Netherlands; <sup>b</sup>Exploration New Ventures, Nexen Petroleum UK Ltd, Uxbridge UB8 1JG, United Kingdom; <sup>c</sup>School of Ocean and Earth Science and Technology, University of Hawai'i at Manoa, Honolulu, HI 96822; <sup>d</sup>Center for Earth Evolution and Dynamics, University of Oslo, NO-0316 Oslo, Norway; <sup>e</sup>Center for Geodynamics, Geological Survey of Norway, NO-7494 Trondheim, Norway; and <sup>f</sup>School of Geosciences, University of the Witwatersrand, Johannesburg WITS 2050, South Africa

Edited by Gerald Schubert, Institute of Geophysics and Planetary Physics, Los Angeles, CA, and approved February 11, 2014 (received for review August 26, 2013)

**Climate trends on timescales of 10s to 100s of millions of years are controlled by changes in solar luminosity, continent distribution, and atmosphere composition. Plate tectonics affect geography, but also atmosphere composition through volcanic degassing of CO<sub>2</sub> at subduction zones and midocean ridges. So far, such degassing estimates were based on reconstructions of ocean floor production for the last 150 My and indirectly, through sea level inversion before 150 My. Here we quantitatively estimate CO<sub>2</sub> degassing by reconstructing lithosphere subduction evolution, using recent advances in combining global plate reconstructions and present-day structure of the mantle. First, we estimate that since the Triassic (250–200 My) until the present, the total paleo-subduction-zone length reached up to ~200% of the present-day value. Comparing our subduction-zone lengths with previously reconstructed ocean-crust production rates over the past 140 My suggests average global subduction rates have been constant, ~6 cm/y: Higher ocean-crust production is associated with longer total subduction length. We compute a strontium isotope record based on subduction-zone length, which agrees well with geological records supporting the validity of our approach: The total subduction-zone length is proportional to the summed arc and ridge volcanic CO<sub>2</sub> production and thereby to global volcanic degassing at plate boundaries. We therefore use our degassing curve as input for the GEOCARBSULF model to estimate atmospheric CO<sub>2</sub> levels since the Triassic. Our calculated CO<sub>2</sub> levels for the mid Mesozoic differ from previous modeling results and are more consistent with available proxy data.**

paleoclimate | carbon cycle | geodynamic

**V**olcanism forms the most efficient mechanism to transfer carbon (C) from the mantle to the ocean–atmosphere system, the exogenic reservoir. At midocean ridges, mantle upwelling occurs between two diverging plates. At subduction zones, sinking oceanic plates lead to arc volcanism (1). A third type of volcanism, driven by mantle plumes, leads occasionally to large igneous provinces (LIPs) that typically last a few My (2, 3). Long-term (>>5 My) changes in volcanic output thus dominantly relate to the long-term plate tectonic processes. Constraints on volcanism-related degassing of CO<sub>2</sub> at subduction zones and midocean ridges hence derive from studies on lithosphere production/consumption (3–6). The quality of these constraints determines the mechanistic underpinning of climatic changes on timescales of 10<sup>7</sup> to 10<sup>8</sup> y. This is because on such timescales, volcanism is the major source of CO<sub>2</sub> to the atmosphere and thereby drives climate and the critical feedbacks in the carbon cycle, such as weathering. To date, estimates of CO<sub>2</sub> degassing through plate tectonic processes for the last 150 My are based on reconstructions of ocean-floor production (7), and for older periods indirect inferences were made through sea level inversion (8). An increasing body of work reveals major uncertainties in eustatic sea level reconstructions, however, based on regional data (9–11).

Over the past two decades, advances have been made in correlation of global plate tectonic reconstructions with mantle structure (e.g., refs. 12–14). Recent work suggest that remnants of the last ~250 My of subduction can still be imaged in seismic tomographic models (15, 16). We apply this to estimate the total imaged subducted lithosphere “slab” length at depth, and from that, paleosubduction zone length at the surface for the past 250 My. Subsequently we compare this to ocean-crust–production rates to assess the associated average subduction rates. In this way, we may obtain a quantitative estimate of lithosphere consumption, and through that, production since the Triassic. To validate our estimates, we compute a global strontium isotope record based on subduction-zone length and test that against the geological record. Finally, we use the thus-obtained lithosphere consumption/production curve as input for the widely used, long-term carbon-cycle model GEOCARBSULF (17) to evaluate the difference in model output with our degassing parameter for estimating atmospheric CO<sub>2</sub> levels, and test these against previous modeling results and available proxy data (18).

## Subduction-Zone Length Evolution

Recently, major elongate P-wave seismic velocity anomalies in the mantle were correlated with locations of former subduction zones (15) in plate tectonic reconstructions using a true polar-wander-corrected paleomagnetic reference frame as basis (19, 20). In a combined analysis of these wave speed anomalies [using the UUP07 tomographic model (21), corroborated by S-wave velocity

## Significance

**Although plate tectonics is generally considered to be the main contributor of CO<sub>2</sub> production, despite decades of paleoproxy and solid-earth research, this very first-order assumption remains unproven. Based on estimates of total subduction-zone lengths, from a combined analysis of seismic tomography models and plate tectonic reconstructions, we have bridged a major gap between solid-earth sciences and the atmosphere and biosphere sciences by providing understanding of one of the most fundamental controls of climate: variation of plate tectonic activity of our planet. By using the subduction zone length input into the GEOCARBSULF climate model, we obtain a better fit with atmospheric CO<sub>2</sub> proxies compared with previously used plate tectonic assumptions.**

Author contributions: D.G.V.D.M. designed research; D.G.V.D.M. and R.E.Z. performed research; D.G.V.D.M., R.E.Z., W.S., and T.H.T. contributed new reagents/analytic tools; D.G.V.D.M. and R.E.Z. analyzed data; and D.G.V.D.M., R.E.Z., D.J.J.v.H., A.S., W.S., and T.H.T. wrote the paper.

The authors declare no conflict of interest.

This article is a PNAS Direct Submission.

<sup>1</sup>To whom correspondence should be addressed. E-mail: douwevdm@gmail.com.

This article contains supporting information online at [www.pnas.org/lookup/suppl/doi:10.1073/pnas.1315657111/-DCSupplemental](http://www.pnas.org/lookup/suppl/doi:10.1073/pnas.1315657111/-DCSupplemental).

anomalies in the independent model S40RTS (22); [Table S1](#)], and geological records of mountain building of the past  $\sim 250$  My, the position and timing of past subduction episodes was determined for 28 major slabs mostly along the continental margins of Pangaea (15). These analyses implied a global average sinking velocity of slabs in the lower mantle of  $1.2 \pm 0.3$  cm/y, yielding a “mantle memory” of subduction of some 250 My (15). Additionally, major intraoceanic subduction within the Panthalassa oceanic realm surrounding Pangaea was identified from the deep mantle structure below, and the geological records around the modern Pacific Ocean (16). These analyses combined resulted in a first-order interpretation of global subduction history and show that all major elongated positive seismic velocity anomalies in the mantle can be consistently matched with former subduction zones, and vice versa. We use this logic to estimate the global subduction-zone-length evolution from seismic tomography. Assuming a constant 1.2 cm/y slab-sinking rate, the global configuration of slabs in a depth section represents the paleo-subduction-zone configuration of an approximate age. To calculate the paleo-subduction-zone length from the lateral slab length measured in a depth section, we compensate the length estimates for volume reduction as a result of mantle phase changes and bulk compression ([Fig. S1](#)). Our interpretations of the top 200 km of the tomographic model, representing late Cenozoic slabs, yield a total subduction zone length of  $\sim 42,400$  km  $\pm 1,300$  km ([Fig. 1A](#), [Table S2](#)), comparing well to the total modern trench length [43,400 km (23) to 48,800 km (24)]. The calculated total subduction-zone length increases to a maximum of  $\sim 75,000$  km at  $\sim 2,000$  km depth ( $\sim 170$  My; [Fig. 1B](#), [Table S2](#)) and decreases to  $\sim 65,500$  km at 2,815 km depth ( $\sim 235$  My; [Fig. 2A](#)). Given the error bar of  $\pm 0.3$  cm/y on the 1.2 cm/y slab-sinking rate (16), the subduction-zone length curve derived here represents an inherently smoothed version of the past. We expect that future studies of individual slabs and tomographic models will be able to estimate the subduction-zone length with ever increasing accuracy.

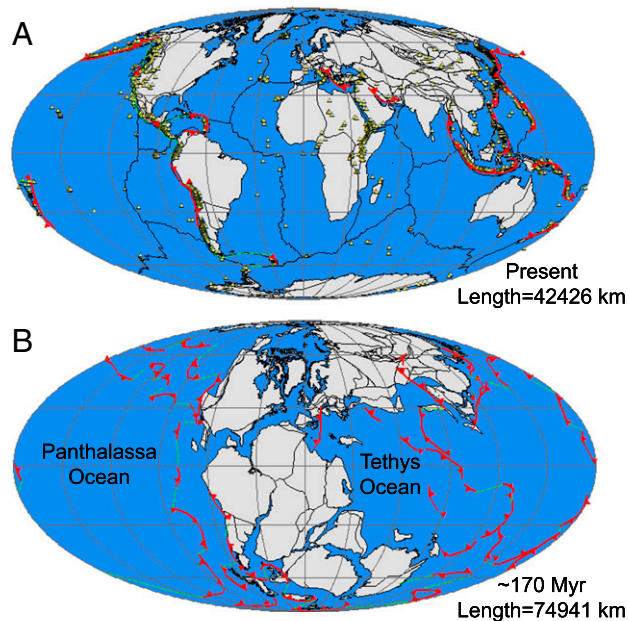


**Fig. 1.** Plate tectonic interpretations of tomographic model; (A) present and (B) 170 My. Red lines with triangles denote interpreted subduction zones (15, 16) from which total subduction zone length is estimated; polarities are speculative. Green lines denote presumed transform zone. Yellow triangles denote present subaerial volcanoes, largely coinciding with subduction zones. Continental blocks in slab-fitted absolute plate reference frame (15).

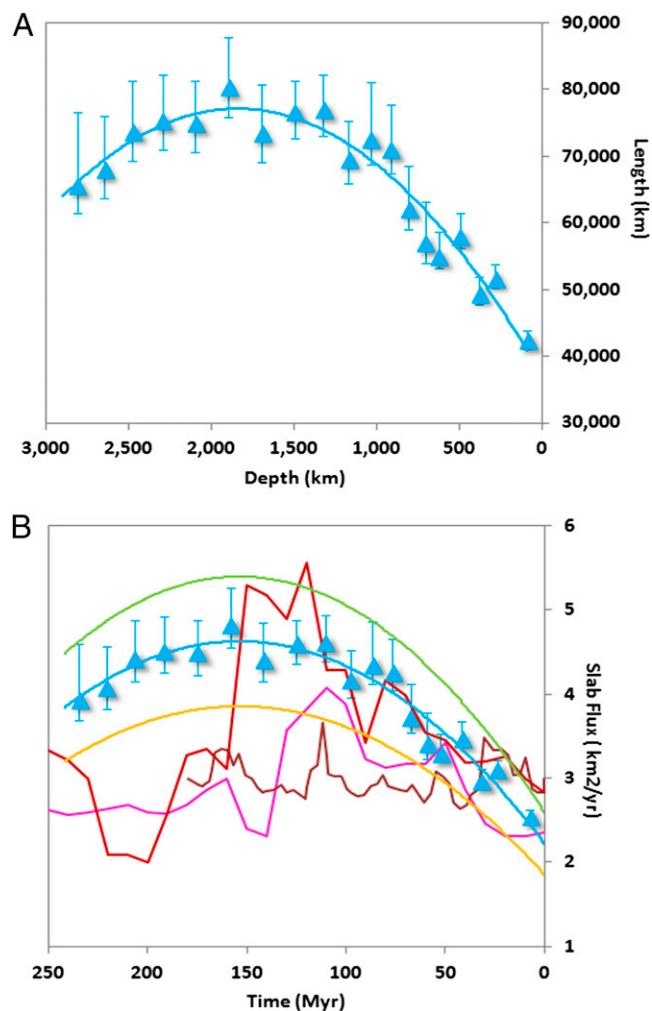


**Fig. 2.** Subduction through time. (A) Calculated total subduction zone length (blue triangles) with error bars. (B) Production rates by midoceanic ridges according to Coltice et al. (32) (red), Rowley (34) (brown), and the standard GEOCARBSULF production rate (purple line) (17). Obtained slab flux (blue triangles) converted to geologic time with 1.2 cm/y slab-sinking rate (15) and polynomials assuming subduction rates of 6 cm/y (blue line, best fit), 5 cm/y (orange line), and 7 cm/y (green line).

The resulting subduction-zone length through time can be described as a simple parabolic function. Increasing total subduction-zone length since the Triassic relates to breakup of Pangaea, when continuous subduction along the circum-Pacific continental margins was established (15, 25, 26) and intraoceanic subduction zones in the Panthalassa Ocean formed (16, 27, 28). Since the mid Jurassic, the total subduction-zone length decreased during collisions in the Tethys Ocean (15, 29, 30) and the Mongol-Okhotsk Ocean (15, 26), and the demise of intraoceanic subduction zones in the Panthalassa Ocean (16), concomitant with growth of the Pacific plate (31, 32).

### Correlation with Mid-Ocean-Ridge Crustal Production

We aim to derive quantitative estimates for plate tectonic volcanic degassing at mid-ocean-ridges (MOR) and arcs combined. Total area consumption at subduction zones per unit time, defined as slab flux (in square kilometers per year) (33), is equal to total area production at oceanic ridges. To test how subduction-zone length (in kilometers) through time is reconciled by area production (in square kilometers per year) through time, we need to multiply

subduction-zone length with a global average subduction rate (centimeters per year).

Marine magnetic anomaly reconstructions have led to two schools of thought for area production rates since the Cretaceous (Fig. 2B). One school interpreted production rates to have not varied significantly (34, 35), the second interprets a decreasing rate (8, 12, 31, 32). The latter scenario served as input for the GEOCARBSULF model for atmospheric CO<sub>2</sub> evolution (17, 18).

Matching our subduction-zone-length curve to the constant area production rate scenario (34, 35) requires that the global average subduction rate increased during the Cenozoic (65–0 My) from ~3–4 to 5.5 cm/y (24) (Fig. S2). Matching the decreasing rate scenario (32), however, requires a constant average subduction rate of  $6 \pm 1$  cm/y (Fig. 2B), i.e., similar to the present day (24). We adopt here a more or less constant global average of subduction rates as we see no geodynamic cause why the process of subduction and the mechanical interaction between slab and mantle should have significantly changed over the past few hundred million years. This may be further illustrated by the observation that the global average of slab-sinking rates appear to be more or less constant since the early Mesozoic (15, 36).

Before 140 My, global MOR-spreading evolution is largely unknown because pre-Cretaceous oceanic crust has almost entirely been subducted (31). We expressed this as “world uncertainty,” the fraction of the earth’s lithosphere that has been subducted since a given time (30), and for which plate motion and configuration at that time is essentially unknown. World uncertainty is ~60% at 140 My, equivalent to 85% uncertainty of the oceanic part of the crust. Global plate models of Mesozoic oceans (31), and calculations based on these, such as for seawater chemistry (37), are based on extrapolation. For pre-Cretaceous time, we therefore prefer to use our total subduction-zone length curve instead, because it is based on (indirect) observation; mantle structure.

In Fig. 2B we show, in addition to the estimates for crustal production (38) and consumption (this paper), the back-calculated crustal production. This is the standard input (7, 8, 39) for the widely used, long-term carbon-cycle model GEOCARBSULF (17, 18). The standard input into GEOCARBSULF curve significantly underestimates the crustal production before 120 My. Applying our curve to GEOCARBSULF will thus likely generate major changes in modeled CO<sub>2</sub> budgets of the pre-120-My world. To test the robustness of our estimates, we will test the predictions of our model for the strontium record.

### Correlation with Strontium Isotope Record

Slab flux (square kilometers per year) has previously been assumed to be proportional to global arc magmatic production rates (kilometers cubed per year; ref. 33), an assumption that may be further supported by our finding that the average subduction rate through time is approximately constant. Our subduction-zone length through time curve (Fig. 2A) is a proxy for slab flux, and may thus constitute a proxy for bulk plate tectonic geochemical input to the exogenic pool since the Triassic. We test this by comparing geologically well-documented Sr isotope ratios (40) with values predicted from our subduction-zone length curve. We use a recent mixing model (41) describing how the <sup>87</sup>Sr/<sup>86</sup>Sr value of the world’s oceans results from mixing inputs of rivers (with higher <sup>87</sup>Sr/<sup>86</sup>Sr) and mantle input from ridge spreading and (weathering) island arcs (with lower <sup>87</sup>Sr/<sup>86</sup>Sr). Scaling the mantle input with our subduction-zone length curve (Fig. S3), we predict a <sup>87</sup>Sr/<sup>86</sup>Sr curve (Fig. 3A) that correlates well with the <sup>87</sup>Sr/<sup>86</sup>Sr curve measured from the geological record (40). This positive test supports our hypothesis that subduction-zone length is a reliable first-order proxy for plate tectonics induced long-term geochemical changes of the global exogenic pool since the Triassic. Our computed curve cannot reproduce second-order variations in the measured <sup>87</sup>Sr/<sup>86</sup>Sr record, which

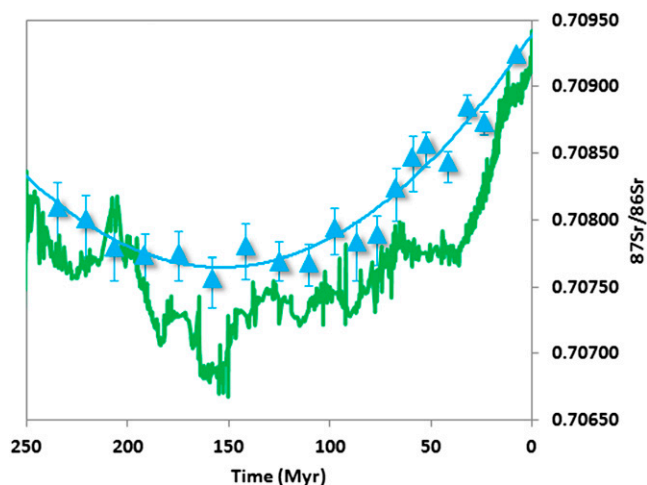


Fig. 3. Corroboration by the strontium record. Green: measured <sup>87</sup>Sr/<sup>86</sup>Sr (40); blue line and triangles: calculated <sup>87</sup>Sr/<sup>86</sup>Sr curve by using our subduction zone-length curve and mixing model (41).

highlights the limitation of our method to variations in fluvial input, i.e., as the result of changing paleogeography (42–44) and to timescales shorter than some 5–20 million years.

### Plate Tectonic Control on CO<sub>2</sub> Production

We now explore the use of our subduction-zone length curve to develop a fully mechanistic proxy of volcanic CO<sub>2</sub> degassing over the Mesozoic and Cenozoic. Upon subduction, most CO<sub>2</sub> is released at depths shallower than 100 km (45), after which it is released to the surface within a few hundred years (46). About 40–70% (47) of the subducted C returns to the exogenic reservoir via volcanism. This occurs within ~2 My after subduction, which is instantaneous on the analyzed timescale (>10 My). The remainder could be introduced to the deep mantle and could be returned to the exogenic reservoir over longer timescales. However, the total carbon budget of the mantle and present-day carbon degassing rates imply a residence time of C in the mantle of >1 and perhaps as long as 4.6 billion years (47). This suggests that once carbon enters the deep mantle, it will unlikely be released as CO<sub>2</sub> as a direct result of subduction-rate variation over the past 250 My (the timescale of our analyses), but will slowly return to the exogenic reservoir, e.g., via partial melting at ridges (48).

The main uncertainty in computing arc CO<sub>2</sub> degassing volumes is carbon concentration of subducting slabs and decarbonation efficiency at subduction zones over time (23). Slab carbon concentrations likely varied through biological evolution and the dynamics of climate and the exogenic carbon cycle—including shelf versus deep ocean carbonate burial, weathering rates, and ocean carbonate chemistry—but the net effect on Phanerozoic slab composition is poorly known. Additional constraints on carbonate production and preservation at the ocean floor through time would refine our flux estimates. For now we here assume constant carbon concentration of subducting lithosphere. Given the constant average global subduction rates, we also assume that decarbonation efficiency, mainly determined by the thermal structure of subduction zones (23), is globally constant.

The carbon degassing from MORs has been estimated to be of similar magnitude as arc volcanism (3, 4, 48), although MORs may be no net contributor, as all CO<sub>2</sub> may be stored locally in hydrothermal carbonates (5). Crustal CO<sub>2</sub> degassing by ridge volcanism occurs by partial melting of the upper mantle up to depths of 330 km (48). As the extent of melted volume depends on the ridge spreading rate (48); at a global level, this translates



to overall crustal area production, which as demonstrated above is directly coupled to the here derived subduction length multiplied with the (constant) subduction rate.

We use the long-term carbon-cycle model GEOCARBSULF (17, 18) to evaluate the effect of our subduction-zone length curve on carbon cycling and atmospheric CO<sub>2</sub> concentrations since the Triassic. In brief, the partial pressure of CO<sub>2</sub> in the atmosphere maintains a long-term flux balance between input and output into and from the exogenic carbon reservoir through the effect of CO<sub>2</sub> on silicate weathering. For instance, an increase in the steady-state degassing rate requires increased weathering and hence higher steady-state *p*CO<sub>2</sub> to balance the fluxes (everything else being equal).

In GEOCARBSULF, the total modern degassing rate due to plate tectonic processes (volcanism, metamorphism, and diagenesis from breakdown of carbonates and organic carbon) is  $7.92 \times 10^{18}$  mol CO<sub>2</sub>/My. Given the constant subduction rate through time, we calculate the total plate tectonic CO<sub>2</sub> degassing through time by scaling the modern degassing rate with our subduction-zone length curve (Fig. 4A). This results in a prediction that CO<sub>2</sub> degassing rose from the Triassic to the mid Jurassic, with a peak CO<sub>2</sub> degassing at ~160 My, followed by a gradual decline to the present (Fig. 4B).

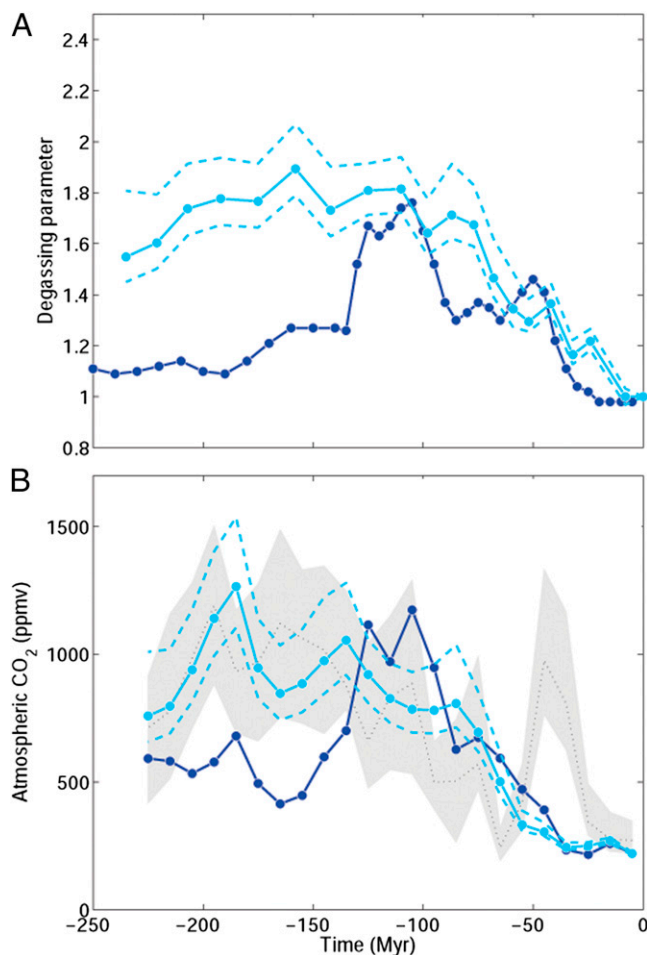


**Fig. 4.** Subduction impacting CO<sub>2</sub> levels. (A) CO<sub>2</sub> degassing parameter, used as input for GEOCARBSULF (17); dark blue: standard GEOCARBSULF degassing parameter (17); light blue: our subduction zone length curve. Dashed lines: error bounds. (B) Atmospheric CO<sub>2</sub> levels, as result of dark blue: NV = 0.013 in ref. 17. Light blue: our study with NV = 0. Gray envelope: proxy data (18), 10-Myr-bin interval.

For the last 120 My, our degassing curve is similar to that of previous work based on marine magnetic anomaly reconstructions (7). For older times, however, where the previous curves used sea level inversion (8), it is distinctly different. We assume that some of the discrepancy can be explained by inaccuracies in the sea level reconstruction (8).

To test the predictive power of both curves, we ran two different configurations of the GEOCARBSULF model, one with standard degassing as described above, the other with our newly obtained degassing parameter (Fig. 4B). In addition, in order to obtain the best match between model-derived *p*CO<sub>2</sub> and proxy records (18) (*Supporting Information*), we optimized a tuning parameter of the model. This tuning parameter (NV; non-volcanic) affects the average value for <sup>87</sup>Sr/<sup>86</sup>Sr of nonvolcanic silicate rocks and ultimately the fraction of Ca-Mg silicate weathering of volcanic rocks relative to nonvolcanic rocks, and may be varied within certain limits (ref. 17 and *Supporting Information*). Although both degassing parameterizations yield similar *p*CO<sub>2</sub> values from ~120 My to the present, our degassing parameterization predicts a gradually changing *p*CO<sub>2</sub> level curve since the Triassic instead of a major increase during the late Jurassic. Our curve appears to be in better agreement with proxy reconstructions (18) (Fig. 4B). For example, a mismatch between the standard GEOCARBSULF results and *p*CO<sub>2</sub> proxies for the mid-Mesozoic was noted earlier by Park and Royer (18) and it was shown that a decrease in weatherable land area in the Jurassic by 50%, would improve the data fit. However, these authors concluded that a 50% reduction in weatherable land area is unreasonably large for this period. In contrast, our degassing approach as presented here reconciles model results and data during the mid Mesozoic without additional assumptions. We note, however, that substantial uncertainties are associated with both the proxy records and the carbon-cycle modeling (4, 17, 18), leading to large discrepancies between models and data during several time periods. It is notable that a major early Cenozoic (50–30 My) peak in the CO<sub>2</sub> curve cannot be explained by plate tectonic processes of either long-term nature: changes in slab flux occur on longer periods, and the effects of LIPS are of shorter term influence. Rather, this peak may relate to effects of orogenesis, e.g., in the Neotethyan or Andean realm. This could imply that CO<sub>2</sub> variations at that time were primarily caused by feedbacks in either continental organic carbon burial (49) or the methane cycle (50), for which carbon and sulfur isotopic evidence exists. Nevertheless, the root mean square error between model-predicted CO<sub>2</sub> and proxy CO<sub>2</sub> values are ~380 ppmv for the standard degassing parameter and ~250 ppmv for our degassing parameter, confirming the better match between model-derived *p*CO<sub>2</sub> and proxy records for the degassing curve derived here.

## Conclusion

In this paper, we quantify global subduction zone length through time since the Triassic using seismic tomographic images of deep mantle relics of subduction zones. Our curve correlates well with ocean production rates if the average global subduction-zone rate was constant, at  $6 \pm 1$  cm/y, which is similar to the modern average subduction rate. We use our results to predict an ocean strontium isotope curve. This curve tests positively against data, showing that our subduction length curve provides a first-order estimate of plate-tectonics-related mantle degassing since the Triassic for timescales of 10–20 My. By applying our subduction length curve to the GEOCARBSULF (17) climate model, we obtain an unprecedented fit between predicted and reconstructed atmospheric CO<sub>2</sub> levels than previous studies, particularly for pre-Cretaceous time. At present, global correlation of seismic tomography models to geological evidence of past subduction is still in its early stages. Increasing resolution in future tomographic models, in combination with more detailed plate reconstructions will constrain the evolution of subduction zones and their individual

volcanic degassing outputs more accurately. Moreover, improved constraints on subducting slab carbon content will refine degassing estimates. We aspire that unlocking the deep mantle record as a data source to quantify global volcanic degassing will further our understanding of the fundamental plate tectonic controls on earth's climate system.

## Materials and Methods

Lower mantle slab remnants were previously (15, 16) inferred from a tomographic model (21), where slab extents were determined based on seismic wave-speed anomaly patterns and where a global paleogeographic context was provided through the reconstructed position of continents in the geologic past. The total lateral slab length was estimated from the tomographic model (21) as a function of depth. These estimates are derived by the comprehensive analysis of one particular P-wave tomographic model (21). Other global tomographic models, based on different data and methods (22, 51–53), are available that generally agree on the presence of large-scale features, but have considerable differences in smaller scales. We used conservative errors of 300–400 km at both endpoints of each interpreted slab anomaly in the lower mantle. Higher degree features are on the scale of this estimated spatial error. The most important issue is the actual existence of the paleosubduction zones in the geological record and the associated slabs in the mantle (15, 16). To test the presence of slabs in a different tomographic model, we compared the mantle anomalies we interpreted in model UU-P07 with the completely independent (in data, model parameterization, and inversion approach) S-wave seismic velocity model S40RTS (22), see Table S1. As this is a first attempt to quantify subduction-zone length from tomographic models, we hope that other groups will follow our approach and analyze their tomographic models in similar ways to provide more estimates of subduction zone length through time.

The errors in the paleosubduction-zone length estimates are primarily dependent on tomographic resolution. Based on previous analyses (15, 16), our the tomographic model has average spatial uncertainties of ~100–200 km in the upper mantle and ~300–400 km in the lower mantle, both in relatively well-imaged regions. In summing slab lengths this propagates into errors of 3–6% of total subduction-zone length in the well-imaged parts of the mantle. However, a more important uncertainty on our estimates of global subduction-zone length stems from parts of the mantle that are insufficiently imaged by seismic tomography. In part, this uncertainty is reduced by knowledge of absence of subduction in the geological record. In plate tectonic reconstructions, continents and oceanic crust without any geological evidence for subduction cover part of the mantle area without sufficient tomographic resolution (paleo-Pacific example shown in Fig. S4). The remaining poorly imaged areas, notably sectors in the former Tethys and Panthalassa oceanic realms, now mostly below the Indian and Pacific Oceans, may have had intraoceanic subduction zones that remain undetected in our tomographic model. These areas are divided by the ratio of the present subduction zone length (~43,000 km) over earth's ocean surface area (~360 × 10<sup>6</sup> km<sup>2</sup>) to arrive at a reasonable estimate maximum error bounds for potentially undetected lengths of paleosubduction zones. The combined errors lead to a potential underestimation of global subduction zone length of up to 17% and may increase the amplitude of the global subduction-zone length curve, but will not change its overall shape.

Because slab material will shrink in volume (3D) with increasing depth as a result of self-compression and phase changes in the mantle, a correction is needed to obtain the initial subduction zone length at surface (Fig. S1). This (1D) correction is computed from mantle density increase with depth of the ak135 earth model (54).

Thickening of slab by pure shear deformation (i.e., without volume change) by factors between 2 and 3 when entering the lower mantle will primarily (55–57) affect the thickness of the anomaly perpendicular to the strike of long subduction zones and does not play a significant role in our estimates of along-strike paleosubduction length. Cooling of the ambient mantle by thermal diffusion may possibly lead to a broader appearance of lower mantle slabs in tomography images. For a thickened slab this is largely dependent on mantle residence time as estimated from thermal modeling of the cooling of instantaneously placed (thickened) slab (57). The first-order effect on our total length estimates would be that we overestimate by ~6% at 100 My and ~10% at 200 My, basically increasing the curvature of our curve in Fig. 2B. The thermal modeling, however, leads to upper estimates (57) and does not account for the counteracting effects during slab sinking of local advection and heating by the dynamic shear flow around the slab. We do not expect thermal diffusion to be critically affecting our paleosubduction length estimates.

Atmospheric CO<sub>2</sub> concentrations were calculated using the long-term carbon-cycle model GEOCARBSULF, including weathering of volcanic rocks (17, 18). A FORTRAN version of the code is available at [http://earth.geology.yale.edu/~jjpark/Code/gcsv10\\_export.f](http://earth.geology.yale.edu/~jjpark/Code/gcsv10_export.f). For all model runs, the following parameter values were used: FERT = 0.4, ACT = 0.09, LIFE = 0.25, GYM = 0.875 (see refs. 4, 17, 18 for details). However, for the two different degassing parameterizations, the model parameter NV was varied. NV affects the average <sup>87</sup>Sr/<sup>86</sup>Sr of nonvolcanic silicate rocks ( $R_{nv}$ ) and ultimately the fraction of Ca-Mg silicate weathering of volcanic rocks ( $X_{volc}$ ) relative to nonvolcanic rocks via the relationship (17):

$$R_{nv} = 0.717 - NV(1 - f_R(t)), \quad [1]$$

where  $f_R(t)$  represents physical erosion over time;  $X_{volc}$  is a function of  $R_{nv}$  (17). NV is an arbitrary parameter that may be varied between reasonable bounds of 0.0 and 0.015, and was optimized here to obtain the best fit between model-derived pCO<sub>2</sub> values and proxy records (ref. 18 and Fig. 4B). We found that NV = 0.013 and NV = 0.0 yields the best fit to CO<sub>2</sub> proxy data for the standard and our degassing parameter, respectively (smallest root mean square error). A value of NV = 0 could suggest that physical erosion has little effect on the volcanic rock weathering fraction. However, we note that NV = 0 only applies to our specific setup (in addition to NV, other parameters could be varied). Moreover, our model runs are restricted to the past 235 My, although the full scope of the GEOCARBSULF model includes the past 570 My. The CO<sub>2</sub> proxy data (18) (average, low, and high) were binned in 10-My intervals. The dotted gray line in Fig. 4B represents average values, and the upper and lower bounds of the light gray envelope indicate low and high values.

**ACKNOWLEDGMENTS.** D.G.V.D.M. thanks the Geological Survey of Norway for its hospitality during his sabbatical in 2009. Part of this work was conducted under programs of the Vening Meinesz School of Geodynamics (Utrecht University) and the Netherlands Research Centre of Integrated Solid Earth Sciences. This work was partly supported by the Research Council of Norway through its Centres of Excellence funding scheme, Project 223272. T.H.T. acknowledges the European Research Council (ERC) under the European Union's Seventh Framework Program (FP7/2007-2013) and ERC Advanced Grant Agreement 267631 (Beyond Plate Tectonics). D.J.J.v.H. and A.S. acknowledge the ERC for Starting Grants 306810 (Subduction Initiation reconstructed from Neotethyan Kinematics) and 259627 (From Protist to Proxy: Dinoflagellates as signal carriers for climate and carbon cycling during past and present extreme climate transitions), respectively. D.J.J.v.H. thanks Netherlands Organization for Scientific Research for a Vidi grant. This paper contributes to the European Science Foundation European Collaborative Research program TOPO-EUROPE.

- Stern RJ (2002) Subduction zones. *Rev Geophys* 40(4):3-1-3-38.
- Svensen H, et al. (2004) Release of methane from a volcanic basin as a mechanism for initial Eocene global warming. *Nature* 429(6991):542-545.
- Marty B, Tolstikhin IN (1998) CO<sub>2</sub> fluxes from mid-ocean ridges, arcs and plumes. *Chem Geol* 145(3-4):233-248.
- Sano Y, Williams SN (1996) Fluxes of mantle and subducted carbon along convergent plate boundaries. *Geophys Res Lett* 23(20):2749-2752.
- Kerrick DM (2001) Present and past nonanthropogenic CO<sub>2</sub> degassing from the solid earth. *Rev Geophys* 39(4):565-585.
- Resing JA, Lupton JE, Feely RA, Lilley MD (2004) CO<sub>2</sub> and 3He in hydrothermal plumes: Implications for mid-ocean ridge CO<sub>2</sub> flux. *Earth Planet Sci Lett* 226(3-4):449-464.
- Engebretson DC, Kelley KP, Cashman HJ, Richards MA (1992) 180 million years of subduction. *Geol Soc Am Today* 2(5):92-95.
- Gaffin S (1987) Ridge volume dependence on seafloor generation rate and inversion using long term sealevel change. *Am J Sci* 287(6):596-611.
- Müller RD, Sdrolias M, Gaina C, Steinberger B, Heine C (2008) Long-term sea-level fluctuations driven by ocean basin dynamics. *Science* 319(5868):1357-1362.
- Sluijs A, et al. (2008) Eustatic variations during the Paleocene-Eocene greenhouse world. *Paleoceanography* 23(4):PA4216.
- Stocchi P, et al. (2013) Relative sea-level rise around East Antarctica during Oligocene glaciation. *Nat Geosci* 6:380-384.
- Richards MA, Engebretson DC (1992) Large-scale mantle convection and the history of subduction. *Nature* 355(6359):437-440.
- Lithgow-Bertelloni C, Richards MA (1998) The dynamics of Cenozoic and Mesozoic plate motions. *Rev Geophys* 36(1):27-78.
- Steinberger B (2000) Slabs in the lower mantle - Results of dynamic modelling compared with tomographic images and the geoid. *Phys Earth Planet Inter* 118(3-4):241-257.
- van der Meer DG, Spakman W, van Hinsbergen DJJ, Amaru ML, Torsvik TH (2010) Towards absolute plate motions constrained by lower-mantle slab remnants. *Nat Geosci* 3:36-40.

16. van der Meer DG, Torsvik TH, Spakman W, van Hinsbergen DJJ, Amaru ML (2012) Intra-Panthalassa Ocean subduction zones revealed by fossil arcs and mantle structure. *Nat Geosci* 5:215–219.
17. Berner RA (2006) Inclusion of the weathering of volcanic rocks in the GEOCARBSULF Model. *Am J Sci* 306(5):295–302.
18. Park J, Royer DL (2011) Geologic constraints on the glacial amplification of Phanerozoic climate sensitivity. *Am J Sci* 211(1):1–26.
19. Torsvik TH, Müller RD, Van der Voo R, Steinberger B, Gaina C (2008) Global plate motion frames: Toward a unified model. *Rev Geophys* 46(3), 10.1029/2007RG000227.
20. Steinberger B, Torsvik TH (2008) Absolute plate motions and true polar wander in the absence of hotspot tracks. *Nature* 452(7187):620–623.
21. Amaru ML (2007) Global travel time tomography with 3-D reference models. PhD dissertation (University of Utrecht, Utrecht, Netherlands).
22. Ritsema J, Deuss A, van Heijst HJ, Woodhouse JH (2011) S40RTS: A degree-40 shear-velocity model for the mantle from new Rayleigh wave dispersion, teleseismic travel-time and normal-mode splitting function measurements. *Geophys J Int* 184(3): 1223–1236.
23. Johnston FKB, Turchyn AV, Edmonds M (2011) Decarbonation efficiency in subduction zones: Implications for warm Cretaceous climates. *Earth Planet Sci Lett* 303(1–2): 143–152.
24. Schellart WP, Freeman J, Stegman DR, Moresi L, May D (2007) Evolution and diversity of subduction zones controlled by slab width. *Nature* 446(7133):308–311.
25. Grand S, van der Hilst RD, Widiyantoro S (1997) Global seismic tomography: A snapshot of convection in the earth. *Geol Soc Am Today* 7:1–7.
26. Van der Voo R, Spakman W, Bijwaard H (1999) Mesozoic subducted slabs under Siberia. *Nature* 397(6716):246–249.
27. Nokleberg WJ, et al. (2000) *Phanerozoic Tectonic Evolution of the Circum-North Pacific*. USGS Professional Paper, Vol 1626.
28. Sigloch K, Mihalynuk MG (2013) Intra-oceanic subduction shaped the assembly of Cordilleran North America. *Nature* 496(7443):50–56.
29. Stampfli GM, et al. (2003) Stratigraphic and Structural Evolution on the Late Carboniferous to Triassic Continental and Marine Successions in Tuscany (Italy). Regional Reports and General Correlation (Bollettino della Società Geologica Italiana, Roma) Vol speciale 2, pp 1–23.
30. Torsvik TH, Steinberger B, Gurnis M, Gaina C (2010) Plate tectonics and net lithosphere rotation over the past 150 My. *Earth Planet Sci Lett* 291(1–4):106–112.
31. Seton M, et al. (2012) Global continental and ocean basin reconstructions since 200 Ma. *Earth Sci Rev* 113(3–4):212–270.
32. Coltice N, Seton M, Rolf T, Müller RD, Tackley PJ (2013) Convergence of tectonic reconstructions and mantle convection models for significant fluctuations in seafloor spreading. *Earth Planet Sci Lett* 383:92–100.
33. Silver PG, Behn MD (2008) Intermittent plate tectonics? *Science* 319(5859):85–88.
34. Rowley DB (2002) Rate of plate creation and destruction: 180 Ma to present. *Geol Soc Am Bull* 114(8):927–933.
35. Cogné J-P, Humler E (2004) Temporal variation of oceanic spreading and crustal production rates during the last 180 My. *Earth Planet Sci Lett* 227(3–4):427–439.
36. Butterworth NP, Talsma AS, Müller RD, Seton M (2014) Geological, tomographic, kinematic and geodynamic constraints on the dynamics of sinking slabs. *J Geodyn* 73:1–13.
37. Müller RD, Dutkiewicz A, Seton M, Gaina C (2013) Seawater chemistry driven by supercontinent assembly, breakup, and dispersal. *Geology* 20:907–910.
38. Müller RD, Sdrolias M, Gaina C, Roest WR (2008) Age, spreading rates, and spreading asymmetry of the world's ocean crust. *Geochem Geophys Geosyst* 9(4), 10.1029/2007GC001743.
39. Berner RA (1994) GEOCARB II: A revised model of atmospheric CO<sub>2</sub> over Phanerozoic time. *Am J Sci* 294(1):56–91.
40. Prokoph A, Shields GA, Veizer J (2008) Compilation and time-series analysis of a marine carbonate [delta]18O, [delta]13C, 87Sr/86Sr and [delta]34S database through Earth history. *Earth Sci Rev* 87(3–4):112–133.
41. Allègre CJ, et al. (2010) The fundamental role of island arc weathering in the oceanic Sr isotope budget. *Earth Planet Sci Lett* 292(1–2):51–56.
42. Otto Bliesner BL (1995) Continental drift, runoff, and weathering feedbacks: Implications from climate model experiments. *J Geophys Res* 100(D6):11537–11548.
43. Gibbs MT, Bluth GJ, Fawcett PJ, Kump LR (1999) Global chemical erosion over the last 250 My: Variations due to changes in paleogeography, paleoclimate, and paleogeology. *Am J Sci* 299(7–9):611–651.
44. Goddés Y, Donnadiou Y, Le Hir G, Lefebvre V (2014) The role of palaeogeography in the Phanerozoic history of atmospheric CO<sub>2</sub> and climate. *Earth Sci Rev* 128:122–138.
45. Gorman PJ, Kerrick DM, Conolly JAD (2006) Modeling open system metamorphic decarbonation of subducting slabs. *Geochem Geophys Geosyst* 7(4):Q04007.
46. John T, et al. (2012) Volcanic arcs fed by rapid pulsed fluid flow through subducting slabs. *Nat Geosci* 5:489–492.
47. Dasgupta R, Hirschmann MM (2010) The deep carbon cycle and melting in Earth's interior. *Earth Planet Sci Lett* 298(1–2):1–13.
48. Dasgupta R, Hirschmann MM (2006) Melting in the Earth's deep upper mantle caused by carbon dioxide. *Nature* 440(7084):659–662.
49. Kurtz AC, Kump LR, Arthur MA, Zachos JC, Paytan A (2003) Early Cenozoic decoupling of the global carbon and sulfur cycles. *Paleoceanography* 18(4):1–14.
50. Dickens GR (2011) Down the rabbit hole: Toward appropriate discussion of methane release from gas hydrate systems during the Paleocene-Eocene thermal maximum and other past hyperthermal events. *Climate of the Past* 7:831–846.
51. Houser C, Masters G, Shearer P, Laske G (2008) Shear and compressional velocity models of the mantle from cluster analysis of long-period waveforms. *Geophys J Int* 174(1):195–212.
52. Simmons NA, Myers SC, Johannesson G, Matzel E (2012) LLNL-G3Dv3: Global P wave tomography model for improved regional and teleseismic travel time prediction. *J Geophys Res* 117(B10):B10302.
53. Li C, van der Hilst RD, Engdahl ER, Burdick S (2008) A new global model for 3-D variations of P-wave velocity in the Earth's mantle. *Geochem Geophys Geosyst* 9(5):Q05018.
54. Kennett BLN, Engdahl ER, Buland R (1995) Constraints on seismic velocities in the Earth from travel times. *Geophys J Int* 122(1):108–124.
55. Gaherty JB, Hager BH (1994) Compositional vs. thermal buoyancy and the evolution of subducted lithosphere. *Geophys Res Lett* 21(2):141–144.
56. Christensen UR (1996) The influence of trench migration on slab penetration into the lower mantle. *Earth Planet Sci Lett* 140(1):27–39.
57. Hafkenscheid E, Wortel MJR, Spakman W (2006) Subduction history of the Tethyan region derived from seismic tomography and tectonic reconstructions. *J Geophys Res* 111(B8):B08401.

# Supporting Information

Van Der Meer et al. 10.1073/pnas.1315657111

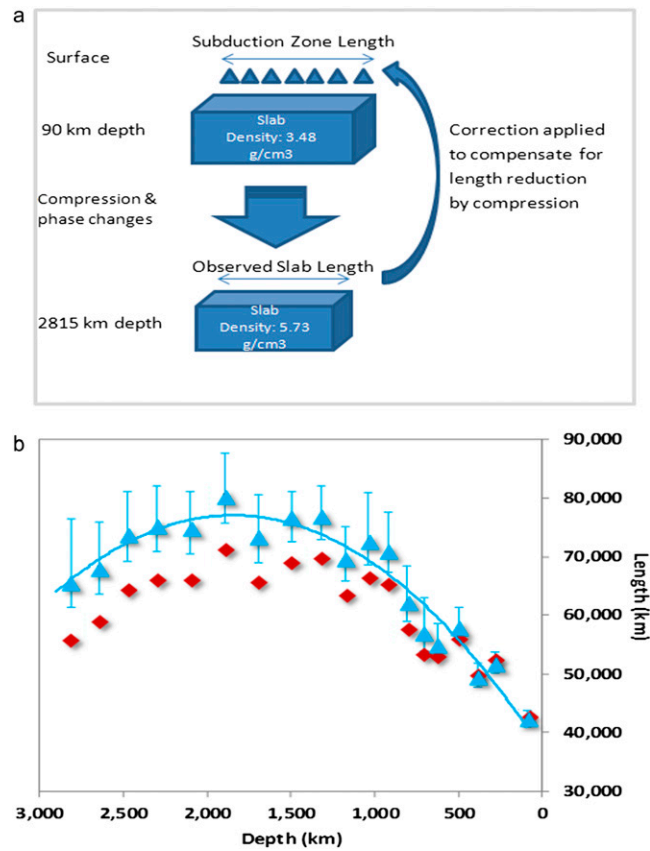


**Fig. S1.** Correction for volume reduction by self compression. (A) Schematic illustrating the correction from observed slab length to subduction-zone length by using the density model (1). (B) Graph illustrating the correction from slab (red diamonds) to subduction-zone length (blue triangles).

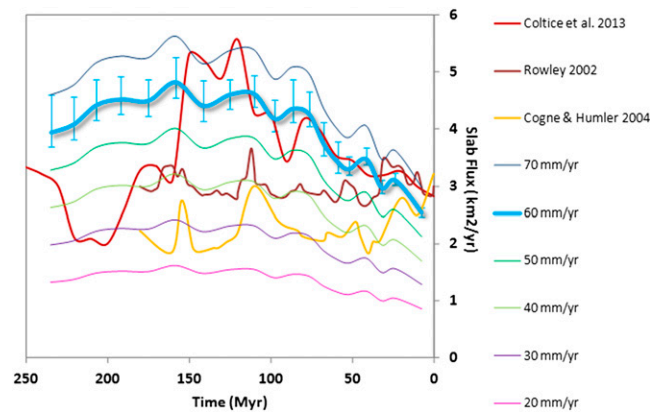


**Fig. S2.** Slab flux through time. Production rates by midoceanic ridges; ref. 2, red; ref. 3, brown; and ref. 4, yellow. Other lines represent the slab flux derived from our subduction length multiplied with various convergence velocities. Bold light-blue line is our best-fit estimate for slab flux including error bars, based on a convergence velocity of 6 cm/yr.







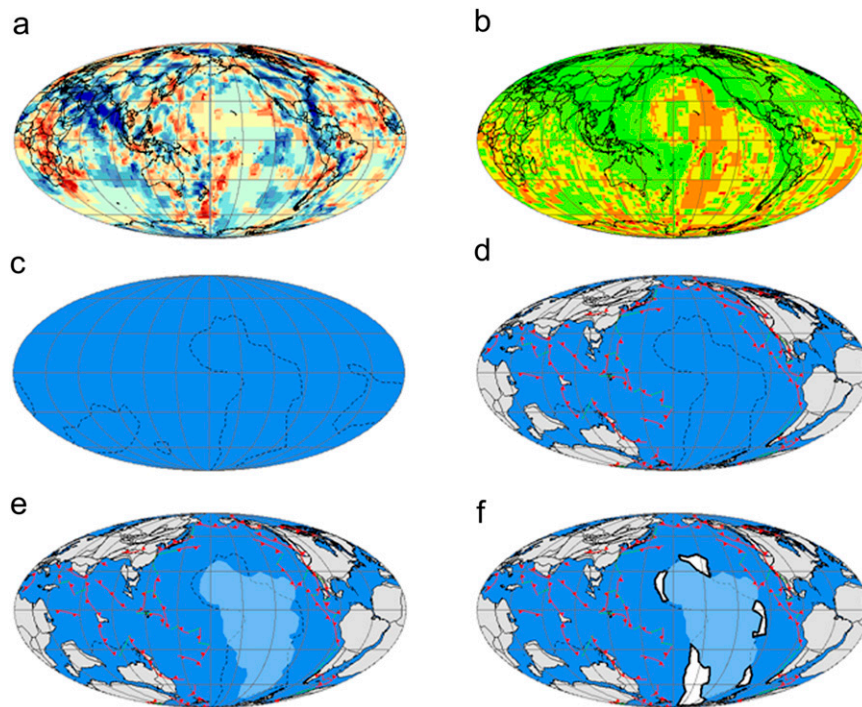


**Fig. 54.** Derivation of subduction-zone length error bounds. Example of (A) slice from tomographic model (5) at 1,500 km depth, and (B) hit count map (5) at 1,500 km depth. Red <100 ray paths/cell; orange (100–500 ray paths/cell); light green (1,000–5,000 ray paths/cell); dark green (5,000+ ray paths/cell); (C) dashed areas; poorly imaged zones (6, 7). (D) Plate tectonic reconstruction (6, 8, 9) of 120 Ma, subduction zone interpretations (6, 7) (red), poorly imaged zone (dashed). (E) Same as C, but with Pacific plates (light blue) with <10 My age uncertainty (10). (F) Remaining areas where slabs are possible, but not imaged (white).

1. Kennett BLN, Engdahl ER, Buland R (1995) Constraints on seismic velocities in the Earth from traveltimes. *Geophys J Int* 122(1):108–124.
2. Coltice N, Seton M, Rolf T, Müller RD, Tackley PJ (2013) Convergence of tectonic reconstructions and mantle convection models for significant fluctuations in seafloor spreading. *Earth Planet Sci Lett* 383:92–100.
3. Rowley DB (2002) Rate of plate creation and destruction: 180 Ma to present. *Geol Soc Am Bull* 114(8):927–933.
4. Cogné J-P, Humler E (2004) Temporal variation of oceanic spreading and crustal production rates during the last 180 My. *Earth Planet Sci Lett* 227(3-4):427–439.
5. Amaru ML (2007) Global travel time tomography with 3-D reference models. PhD dissertation (University of Utrecht, Utrecht, Netherlands).
6. van der Meer DG, Spakman W, van Hinsbergen DJJ, Amaru ML, Torsvik TH (2010) Towards absolute plate motions constrained by lower-mantle slab remnants. *Nat Geosci* 3:36–40.
7. van der Meer DG, Torsvik TH, Spakman W, van Hinsbergen DJJ, Amaru ML (2012) Intra-Panthalassa Ocean subduction zones revealed by fossil arcs and mantle structure. *Nat Geosci* 5:215–219.
8. Torsvik TH, Müller RD, Van der Voo R, Steinberger B, Gaina C (2008) Global plate motion frames: Toward a unified model. *Rev Geophys* 46(3):1–44.
9. Steinberger B, Torsvik TH (2008) Absolute plate motions and true polar wander in the absence of hotspot tracks. *Nature* 452(7187):620–623.
10. Müller RD, Sdrolias M, Gaina C, Steinberger B, Heine C (2008) Long-term sea-level fluctuations driven by ocean basin dynamics. *Science* 319(5868):1357–1362.
11. Allegre CJ, et al. (2010) The fundamental role of island arc weathering in the oceanic Sr isotope budget. *Earth Planet Sci Lett* 292(1):51–56.

**Table S1. Slab data table**

Abbreviation	Slab name	Slab depth				Slab midpoint		
		Base		Top		Depth	Lon	Lat
		Min	Max	Min	Max			
Aeg	Aegean Tethys	2,100	1,900	0	0	1,000	26.0	42.0
Ag	Algeria	2,300	2,100	1,500	1,325	1,806	7.0	24.0
Al	Aleutian	810	710	0	0	380	-165.0	57.0
At	Atlantis	2,900	2,815	2,650	2,480	2,711	-39.0	22.0
Ba	Balkan	2,900	2,815	2,650	2,480	2,711	17.0	47.0
Bf	Beaufort	2,815	2,650	2,300	2,100	2,466	-128.0	72.0
Ca	Caribbean	810	710	0	0	380	-63.0	13.0
CC	Central China	2,900	2,815	1,500	1,325	2,135	88.0	45.0
Ch	Chukchi	1,900	1,700	1,175	1,040	1,454	170.0	77.0
EC	East China	2,900	2,815	1,700	1,500	2,229	128.0	43.0
Eg	Egypt	2,300	2,100	920	810	1,533	31.0	32.0
Far	Farallon	2,650	2,480	920	710	1,690	-73.0	35.0
GI	Georgia Islands	2,900	2,815	1,500	1,325	2,135	-30.0	-56.0
Hi	Himalayas	1,175	1,040	500	440	789	78.0	26.0
Id	Idaho	2,480	2,300	810	710	1,575	-118.0	49.0
Kc	Kamchatka	1,040	920	0	0	490	155.0	55.0
Mc	Manchuria	1,040	920	0	0	490	135.0	46.0
Md	Maldives	2,100	1,900	560	500	1,265	79.0	14.0
Me	Mesopotamia	2,300	2,100	1,325	1,175	1,725	46.0	33.0
Mg	Mongolia	2,100	1,900	1,175	1,040	1,554	120.0	48.6
MO	Mongol-Okhotsk	2,900	2,815	1,900	1,700	2,329	76.0	67.0
NP	North Pacific	1,500	1,325	850	760	1,109	-143.0	56.0
Ro	Rockall	2,900	2,815	2,650	2,480	2,711	-13.0	57.0
Sa	Sakhalin	1,175	1,040	710	625	888	135.0	55.4
So	Socorro	2,300	2,100	810	710	1,480	-108.0	17.0
TA	Trans Americas	2,900	2,815	2,480	2,300	2,624	-67.0	2.0
Ve	Venezuela	1,500	1,325	810	710	1,086	-67.0	2.0
Wc	Wichita	2,815	2,650	2,100	1,900	2,366	-98.0	37.0
Te1	Telkhinia1	2,480	2,300	2,100	1,900	2,195	178.0	14.0
Te2	Telkhinia2	2,300	2,100	1,700	1,500	1,900	179.0	5.0
Te3	Telkhinia3	1,700	1,500	1,500	1,175	1,469	-177.0	-2.0
Te4	Telkhinia4	2,900	2,815	2,300	2,100	2,529	164.0	34.0

**Table S2. Subduction-zone length data**

Depth (km)	Age (My)	Lateral slab length (km)	Tomographic				SBZ length	SBZ length error (km)	Poor imaging zones error (km)	Combined error root sum of squares	SBZ length ratio average	SBZ length ratio minimum	SBZ length ratio maximum
			spatial error (km)	Slab count	Shrinkage factor	SBZ length							
90	8	42,672	200	23	0.99	42,426	1,349	0	1,349	1.000	0.968	1.032	
285	24	52,465	200	28	0.99	51,686	1,474	1,410	2,040	1.218	1.184	1.266	
385	32	49,770	200	33	0.99	49,478	1,615	1,787	2,409	1.166	1.128	1.223	
500	42	55,992	200	33	1.03	57,925	1,681	3,007	3,445	1.365	1.326	1.447	
628	52	53,119	200	31	1.03	54,936	1,629	3,423	3,791	1.295	1.256	1.384	
710	59	53,469	400	26	1.07	57,021	3,076	5,182	6,026	1.344	1.272	1.486	
810	68	57,784	400	27	1.08	62,160	3,162	5,654	6,478	1.465	1.391	1.618	
920	77	65,464	400	35	1.09	71,032	3,631	5,548	6,631	1.674	1.589	1.831	
1,040	87	66,544	400	39	1.09	72,641	3,856	7,609	8,530	1.712	1.621	1.913	
1,175	98	63,464	400	34	1.10	69,644	3,620	4,425	5,717	1.642	1.556	1.776	
1,325	110	69,785	400	40	1.10	77,013	3,948	3,500	5,276	1.815	1.722	1.940	
1,500	125	69,095	400	42	1.11	76,736	4,071	1,895	4,491	1.809	1.713	1.915	
1,700	142	65,688	400	47	1.12	73,459	4,337	5,842	7,276	1.731	1.629	1.903	
1,900	158	71,381	400	49	1.13	80,352	4,457	5,903	7,397	1.894	1.789	2.068	
2,100	175	66,158	400	47	1.13	74,941	4,393	4,516	6,300	1.766	1.663	1.915	
2,300	192	66,119	400	46	1.14	75,345	4,372	5,244	6,827	1.776	1.673	1.937	
2,480	207	64,357	400	48	1.15	73,714	4,489	5,986	7,482	1.737	1.632	1.914	
2,650	221	59,097	400	43	1.15	68,004	4,269	6,843	8,065	1.603	1.502	1.793	
2,815	235	55,934	400	39	1.17	65,659	4,147	10,235	11,043	1.548	1.450	1.808	

SBZ, subduction-zone length.